Theoretical dissection of the electronic anisotropy and quantum transport of ultrascaled halogenated borophene MOSFETs

Shiying Guo,[1,2] Ying Wang,[1] Hengze Qu,[2] Wenhan Zhou,[2] Yee Sin Ang ◉,[3,*] Shengli Zhang,[2,†] and Haibo Zeng[2,‡]

[1]*College of Physics Science and Technology, Yangzhou University, Yangzhou 225002, China*

[2]*MIIT Key Laboratory of Advanced Display Materials and Devices, School of Materials Science and Engineering, Nanjing University of Science and Technology, Nanjing 210094, China*

[3]*Science, Mathematics and Technology, Singapore University of Technology and Design, Singapore 487372, Singapore*

Two-dimensional (2D) anisotropic semiconductors, such as black phosphorene, show strong potential in ultrascaled metal-oxide-semiconductor field-effect transistors (MOSFETs) as the anisotropic electronic structure is highly beneficial in boosting the device performance at sub-10-nm gate length regime. Metallic graphenelike borophene can be halogenated to form a stable monolayer family of B_4X_4 (X = F, Cl, and Br) whose highly anisotropic semiconducting electronic structures suggest a potential in ultrascaled MOSFET applications. Here, we computationally explore the quantum transport properties of B_4X_4 monolayers as high-performance (HP) 5-nm MOSFETs. The HP ON-state current of the *n*-type 5-nm monolayer B_4X_4 MOSFETs can reach over 3000 μA/μm at 5-nm gate length regime, thus fulfilling the ITRS requirement of HP devices. Of note, by analyzing the physical relationship between the anisotropic electronic structures (transport effective mass $m_{//}$ and density of states m_{DOS}), we show that large electronic anisotropy does not immediately guarantee high performance. An overly large $m_{//}$ or m_{DOS} would suppress the saturation current and lead to limited HP ON-state current of monolayer B_4X_4, thus revealing a balance between the effective masses is needed when designing 2D semiconductor MOSFETs. This work provides insights and design guidelines for the development of next-generation nanoelectronic devices based on the exceptional transport properties of 2D anisotropic channel materials.

I. INTRODUCTION

The continuous shrinking of silicon-based metal-oxide-semiconductor field-effect transistors (MOSFETs) below 10-nm gate length is tremendously challenging due to the inherent physical limits of silicon [1,2]. Two-dimensional (2D) semiconductors are attractive candidates for future logic devices benefitting from their atomic-thickness and dangling-bond-free surfaces, which can circumvent the short-channel effect that plagues most bulk semiconductors [3–5]. Numerous MOSFETs based on 2D semiconductors have been investigated recently, including 2D MoS_2 [6,7], InSe [8,9], and Bi_2O_2Se [10]. Interestingly, 2D semiconductors with anisotropic electronic structures, such as black phosphorene [11,12], 2D group VA-VA monolayers [13–15], and niobium oxyhalides [16–19], tend to exhibit considerably higher ON-state currents [20–22], and thus are promising for nanoelectronic device applications. The anisotropic electronic structure signifies that the band dispersion around valence-band maximum (VBM) and conduction-band minimum (CBM) are anisotropic along different in-plane directions. Black phosphorene is a particularly attractive electronically anisotropic 2D semiconductor channel material. Black phosphorene MOSFETs can achieve a high ON-state current (approximately 4000 μA/μm) and fast switching speed even when the channel length is shortened below 10 nm [12,23]. The practicality of black phosphorene in device applications is, however, severely impeded by its chemical instability under ambient condition [24]. The search for stable and anisotropic 2D semiconductors beyond black phsophorene remains an open quest thus far.

2D borophene, a monolayer composed dominantly of boron atoms, represents another emerging 2D family in which a large variety of distinctive allotropes are available due to the diverse bonding configurations of boron [25–30]. Among the numerous allotropes of borophene, the existence of graphenelike borophene has been intensively studied [31]. Free-standing graphenelike borophene with only three valence electrons cannot form

---

*Corresponding author: yeesin_ang@sutd.edu.sg

†Corresponding author: zhangslvip@njust.edu.cn

‡Corresponding author: zeng.haibo@njust.edu.cn

a large π bond to stabilize the atomic structure. Nevertheless, such graphenelike borophene can be well stabilized using functional groups such as H, F, and O to provide excess electrons [32–35]. Experimentally, hydrogenated boride sheets are successfully prepared based on exfoliation and ion-exchange processes [36,37]. Additionally, surface halogenation can effectively open a sizable band gap in such graphenelike borophene (i.e., B_4F_4, B_4Cl_4, and B_4Br_4) [32,38]. The stability of halogenated borophene is substantially improved as compared to the pristine graphenelike borophene. Of note, halogenated borophene exhibits an anisotropic electronic structure, which is possible to obtain a high ON current for nanoelectronics [32]. It is thus of great interest and technological significance to investigate the potential of the halogenated borophene as a channel material in ultrascaled MOSFETs and to understand the relationship between their anisotropic electronic structures and the performance limit.

In this work, we computationally study the transport properties of 5-nm gate-length *n*- and *p*-type high-performance (HP) MOSFETs based on monolayer B_4X_4 with anisotropic electronic structures. The band gaps of monolayer B_4F_4, B_4Cl_4, and B_4Br_4 are 0.70, 1.39, and 1.19 eV, respectively. The small band gap of monolayer B_4F_4 could be enlarged by strain engineering, thus effectively suppressing the OFF-state leakage current below 0.1 µA/µm while boosting the ON-state current to 3140 µA/µm. Significantly, our analysis reveals a physical relationship between the anisotropic electronic structures and the HP ON-state current. Here overly large transport effective mass $m_{//}$ and density of states m_{DOS} lead to a reduced carrier injection velocity and small saturation current, thus severely restricting the ON-state current. Our findings provide useful insights on the design guidelines of optimal 2D semiconducting channel materials and shed light on the underlying transport mechanisms that are beneficial for improving device performance, thus providing a key step towards the development of HP MOSFET device technology beyond the silicon era.

II. COMPUTATIONAL METHODS

All structural optimization and electronic structure calculations are performed by density-functional theory (DFT). Perdew-Burke-Ernzerhof (PBE) functional under generalized gradient approximation (GGA) is used to describe the exchange-correlation function [39]. A 38-Å vacuum space is included to eliminate the interaction between the periodic layers. The Brillouin zone is sampled using $30 \times 30 \times 1$ Monkhorst-Pack *k* points [40]. The quantum transport is simulated by using a method of DFT combined with the nonequilibrium Green's function (NEGF) [41]. The drain current I_{ds} is calculated based on

the Landauer-Bűttiker formula [42,43]

$$I_{ds} = \frac{2e}{h} \int_{-\infty}^{+\infty} \{T(E)[f_s(E - \mu_s) - f_d(E - \mu_d)]\}dE, \quad (1)$$

where $T(E)$, f_{s-d}, and μ_{s-d} are the transmission function, the Fermi-Dirac distribution functions for the source and drain, and the electrochemical potentials of the source and drain, respectively. The cutoff energy is 80 hartree. The simulated temperature is 300 K. All calculations are performed in the QuantumATK package [44].

III. RESULTS AND DISCUSSION

Top and side views of monolayer B_4X_4 geometric structure are shown in Fig. 1(a), which is obtained by the surface halogenation of graphenelike borophene. For comparison, the optimized graphenelike borophene is shown in Fig. S1 within the Supplemental Material [64] with the lattice constant of 2.95 Å, which is in good agreement with the result of the literature [32]. The surface halogenation of graphenelike borophene induces the partial B—B bond breaking, accompanied by the space-group symmetry changing from *Cmmm* to *P6/mmm*. Thus, the isotropic atomic structure becomes anisotropic. The B atoms are still in the same plane but sandwiched between two layers of X atoms, arranged in a square lattice. The lattice constants of *a* and *b* are summarized in Table SI within the Supplemental Material [64], which are consistent with the results of previously reported works [32,38]. The stability of monolayer B_4X_4 is attributed to the formation of three-center two-electron ($3c$—$2e$) bond (B—X—B bonds), as shown in Fig. 1(b). The B—B covalent bonds are the classical two-center two-electron ($2c$—$2e$) bond. In addition, we further compute the phonon dispersion of monolayer B_4X_4 as shown in Fig. S2 within the Supplemental Material [64]. No imaginary modes are observed in the first Brillouin zone for all monolayer B_4X_4, indicating their dynamic stability.

The electronic band structures of monolayer B_4X_4 are calculated along the high-symmetry path in the orthogonal Brillouin zone, as shown in Figs. 1(c)–1(f). The band gap is opened as a result of the surface halogenation and the band gaps of monolayer B_4F_4, B_4Cl_4, and B_4Br_4 are 0.70, 1.39, and 1.19 eV, respectively. The VBM and CBM are both located at the Γ point, leading to the direct band gap. Monolayer B_4Cl_4 has the maximum band gap among them, which can be explained by the projected density of states (PDOS). As plotted in the PDOS of Figs. 1(d)–1(f), the VBM of monolayer B_4X_4 is dominated by the p_x orbitals of the B atom and the p_x orbitals of the halogen atom. However, the B-p_x orbitals play a leading role for the VBM of monolayer B_4F_4, while the F-p_x orbitals contribute to a lesser degree to the VBM. The PDOS near the VBM further confirms that the in-plane bonding states
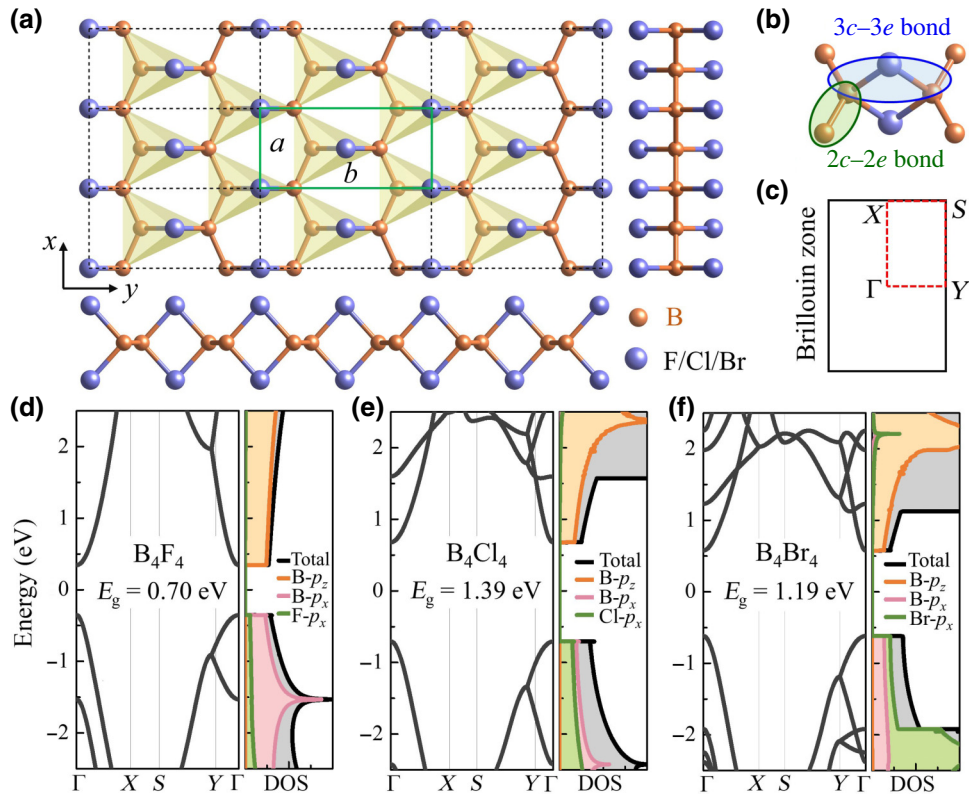
FIG. 1. The (a) atomic structure, (b) $3c$—$2e$ bond and $2c$—$2e$ bond, (c) Brillouin zone, (d)–(f) band structure and projected density of states (PDOS) of monolayer B_4X_4.

are fully filled after surface halogenation, resulting in the stable monolayer B_4X_4 structure [32,45,46]. The partial charge density distribution of the VBM in Fig. S3 within the Supplemental Material [64] clearly reveals the in-plane bonding states including B-p_x orbitals and X-p_x orbitals. The CBM of monolayer B_4X_4 is mainly dominated by the B-p_z orbitals. In addition, the CBM is also composed of the sp hybridization from the s orbitals and p_z orbitals of the halogen atom.

To gain insight on the energy-dispersion relationship near the VBM and CBM, we highlight the band dispersion and effective mass along the x and y directions of monolayer B_4X_4 in Fig. 2. The band dispersion near the CBM along the x direction is weaker than that along the y direction [see Fig. 2(a)], corresponding to the heavy m_x and light m_y [see Fig. 2(b)]. For the VBM, the energy dispersion along the x direction is stronger [Fig. 2(d)], corresponding to the lighter m_x in Fig. 2(e). The band dispersion along the y direction is weaker, and the corresponding m_y is heavier. In addition, both the m_x and m_y of monolayer B_4X_4 determines the density of states (DOS). The DOS of channel materials has a significant impact on the carrier injection and ON-state current of MOSFETs [47,48]. In order to quantify their DOS for convenient comparison, we define the effective mass of the DOS as $m_{DOS} = (m_x \times m_y)^{1/2}$, as shown in Figs. 2(c) and 2(f). The calculated values of the

effective mass and m_{DOS} can be found in Table SII within the Supplemental Material [64].

The anisotropic electronic properties of the monolayer B_4X_4 crucially influence their quantum transport characteristics in the double-gate MOSFET device configuration. The device configuration of a monolayer B_4X_4 MOSFET is shown in Fig. 3(a). Monolayer B_4X_4 is sandwiched between the dielectric layer of SiO_2 with the dielectric constant of 3.9 and the thickness of 0.41 nm. Both the channel length and gate length are 5 nm without underlap structure as shown in Fig. S4 within the Supplemental Material [64]. The thickness value is adopted from the International Technology Roadmap for Semiconductors (ITRS) requirements at the 5-nm channel length [49,50]. The highly doped monolayer B_4X_4 acts as the source and drain and the optimal electrode doping is 5×10^{13} cm^{-2} in accordance with the HP device requirements of ITRS. The doping concentration of electrode is possible to be realized in 2D-layered materials based on several doping strategies, such as electrostatic doping [51,52], surface charge transfer [53–55], and modulation doping [56,57].

The ON-state current, which can be extracted from the transfer characteristics curves, is a critical parameter for the logic switching applications, especially for the HP devices where a high ON-state current is desirable for achieving fast operation speed. Figures 3(b)–3(e) show the
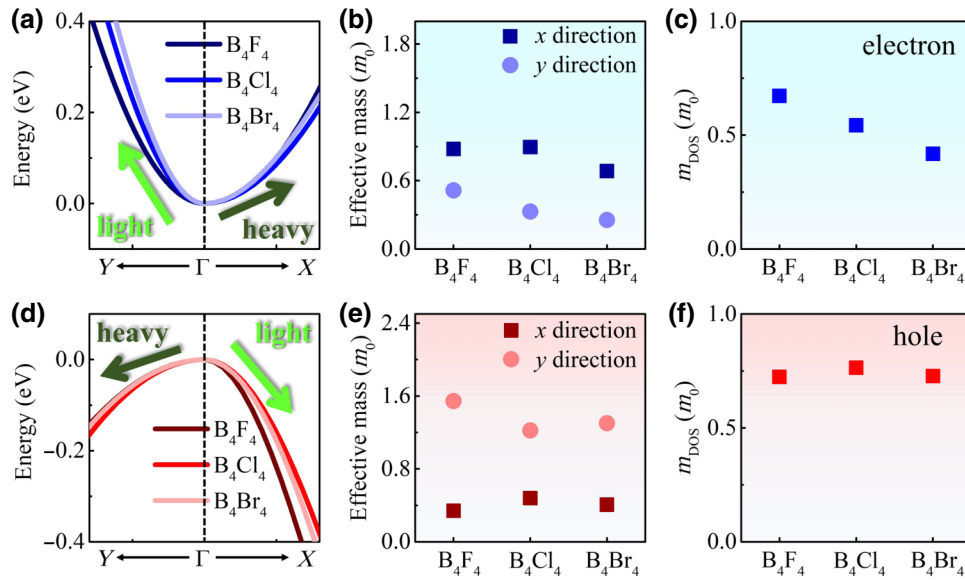
FIG. 2. The (a) band dispersion near the CBM, (b) electron effective mass, and (c) corresponding density of states effective mass (m_{DOS}) for monolayer B_4X_4. The (d) band dispersion near the VBM, (e) hole effective mass, and (f) corresponding m_{DOS} for monolayer B_4X_4.

transfer characteristic curves of 5-nm gate-length monolayer B_4X_4 MOSFETs. The ON-state current is acquired at a gate voltage of V_g (ON) $= V_g$ (OFF) $+ V_{dd}$, where V_{dd} is the supply voltage and V_g (OFF) is the OFF-state voltage. According to ITRS requirements for HP devices, the OFF-state current is set to 0.1 μA/μm, as shown in Figs. 3(b)–3(e). For monolayer B_4Cl_4 and B_4Br_4, the ON-state current of the *n*-type and *p*-type MOSFETs can meet the ITRS standard because their suitable band gaps and appropriate anisotropic effective masses (see Table SIII within the Supplemental Material [64]). The ON-state current of the *n*-type monolayer B_4Cl_4 and B_4Br_4 MOSFETs along the *y* direction reaches up to 3670 and 3180 μA/μm, respectively. However, the ON-state current of monolayer B_4F_4 MOSFETs is lower than the ITRS standard of 900 μA/μm, which is caused by the small band gap of monolayer B_4F_4.

To understand how the band gap affects the transport properties and device performance, we calculate the transfer characteristics of the MOSFETs based on monolayer B_4F_4 under 5% compressive strain along the *y* axis, as shown in Fig. S5 within the Supplemental Material [64]. Applying 5% compressive strain along the *y* axis of monolayer B_4F_4 yields a suitable band gap of 1.19 eV, with the invariable anisotropy of the effective masses. The electrode doping concentration of monolayer strained-B_4F_4 MOSFETs is also 5×10^{13} cm^{-2}. As shown in Fig. S5 within the Supplemental Material [64], the source-to-drain leakage tunneling of monolayer strained-B_4F_4 MOSFETs is significantly weakened, and the leakage current is greatly reduced. Such leakage current reduction originates from the increased band gap of monolayer strained B_4F_4.

Position-resolved local density of states (PLDOS) further demonstrates the transmission mechanism of leakage current reduction, as shown in Figs. 3(f) and 3(g). The barrier height (Φ_B) increases from 0 to 0.15 eV when the band gap increases, effectively preventing electron tunneling and thus inhibiting leakage current. According to the fixed I_{OFF} and V_{dd} of the ITRS HP requirements, the attainable ON-state current of monolayer strained-B_4F_4 MOSFETs also increases significantly, as shown in Fig. 3(h). The ON-state current of *n*-type *y*-directed MOSFETs increases from 600 to 3140 μA/μm (see Tables SIII and SIV within the Supplemental Material [64]).

Subthreshold swing (SS) is another key figure of merit for evaluating the gate electrostatic control capability of a logic device. SS is defined as the gate voltage required to change the current by a factor of 10 [58],

$$\mathrm{SS} = \frac{\partial V_g}{\partial \log I_{ds}}. \tag{2}$$

A smaller SS corresponds to a better gating efficiency [59]. The SS of monolayer B_4F_4 MOSFETs is reduced after increasing the band gap [see Fig. 3(i)]. The SS of the *n*-type MOSFET along the *y* direction decreases dramatically from 141 to 81 mV/dec, thus suggesting strain engineering as an effective approach to improve the switching characteristics of the MOSFET.

The performances of monolayer B_4X_4 MOSFETs are expected to be sensitively influenced by the band gaps and effective mass values. We further elucidate how such factors can affect the device performance in Fig. 4. The saturation current I_{sat} is the upper limit of the current of
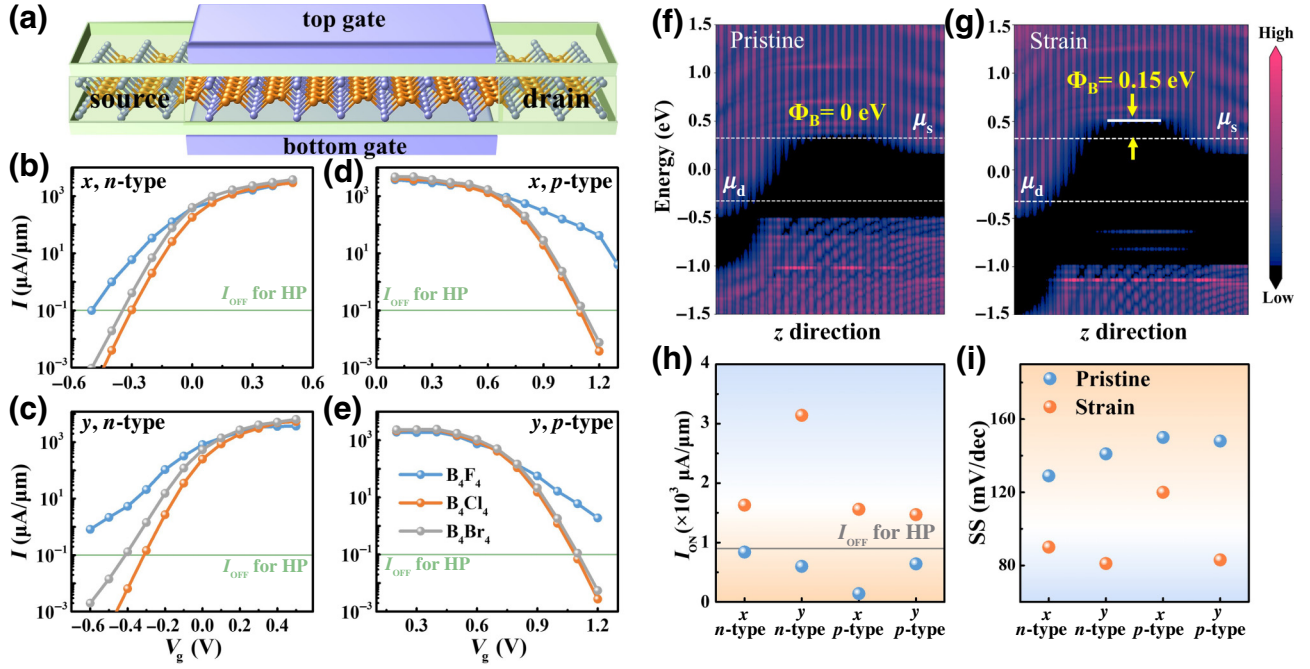
FIG. 3.   The (a) device configuration and (b)–(e) transfer characteristics of 5-nm gate-length MOSFETs based on monolayer B_4X_4. The light green horizontal line represents the ITRS HP requirements for the OFF-state current ($I_{OFF} = 0.1$ µA/µm). The source-drain voltage $V_{ds} = 0.65$ V, which is equal to the supply voltage (V_{dd}). (f),(g) Position-resolved local density of states (PLDOS) at $V_g = -0.314$ V. The n-type y-directed strained-B4F4 MOSFET obtains the I_{OFF} of 0.1 µA/µm at $V_g = -0.314$ V. (h) SS, and (i) I_{ON} of the MOSFETs based on monolayer pristine B_4F_4 and monolayer strained B_4F_4. The gray horizontal line represents the ITRS HP requirements for the ON-state current ($I_{ON} = 900$ µA/µm).

MOSFETs. In the case of ballistic transport, I_{sat} is proportional to the carrier injection velocity υ_{inj} from the source [13,60]. Here, the υ_{inj} can be expressed as

$$\upsilon_{inj} \propto \frac{N_s}{m_{DOS} \times m_x}^{1/2}, \quad (3)$$

where N_s is the surface carrier concentration. Equation (3) shows that the saturation current I_{sat} is proportional to $(m_{DOS} \times m_x)^{-1/2}$. The saturation current I_{sat} of monolayer B_4X_4 MOSFETs is extracted from the I-V curve, which is the highest current. We calculate $(m_{DOS} \times m_{//})^{-1/2}$ of monolayer B_4X_4 MOSFETs, where $m_{//}$ is the effective mass parallel to the transmission direction. An excellent linear relationship between the I_{sat} and $(m_{DOS} \times m_{//})^{-1/2}$ is shown in Fig. 4(a). Notably, Fig. 4(a) reveals that 2D semiconductors with overly large m_{DOS} or $m_{//}$ are undesirable for MOSFET applications due to the limited magnitude of the ON-state current. Additionally, the excellent linear relationship between the I_{sat} and $(m_{DOS} \times m_{//})^{-1/2}$ in Fig. 4(a) is independent of the different band gaps of monolayer B_4X_4. Therefore, we can find that the size of the band gap has minimal influence on I_{sat}.

In order to investigate how the anisotropy of the effective mass affects the ON-state current, we display the relationship between the ON-state current, the parallel effective mass $m_{//}$ and the vertical effective mass $m_{\perp}$ of monolayer B_4X_4. The vertical effective mass $m_{\perp}$ is the effective mass vertical to the transmission direction. As shown in Fig. 4(b), for monolayer B_4X_4 with larger $m_{//}$ or $m_{\perp}$, the ON-state current is reduced. For example, monolayer strained B_4F_4 with a large y-directional hole effective mass of 1.8 m_0 has a relatively low ON-state current of approximately 1500 µA/µm. Conversely, the ON-state current of the n-type B_4X_4 MOSFETs along the y direction is relatively higher due to their relatively smaller $m_{//}$ values (0.255–0.519 m_0) and appropriate $m_{\perp}$ values (0.684–0.896 m_0). Such behaviors highlight a key channel material selection rule for 2D-semiconductor-based transistor applications: *a greater degree of anisotropy does not necessarily correspond to a better device performance.* Instead, a better performance requires *a smaller parallel effective mass while the vertical effective mass cannot be overly large*.

We further calculate the relationship between the SS and the band-gap value E_g as well as the parallel effective mass $m_{//}$ of monolayer B_4X_4 MOSFETs, as shown in Fig. S6 within the Supplemental Material [64]. Unlike the saturation current, the magnitude of the SS is affected by E_g. An excessively small value of the band gap (such as 0.70 eV for monolayer B_4F_4) suffer from a large leakage current, and thus degrade SS and the gainable ON-state current for a
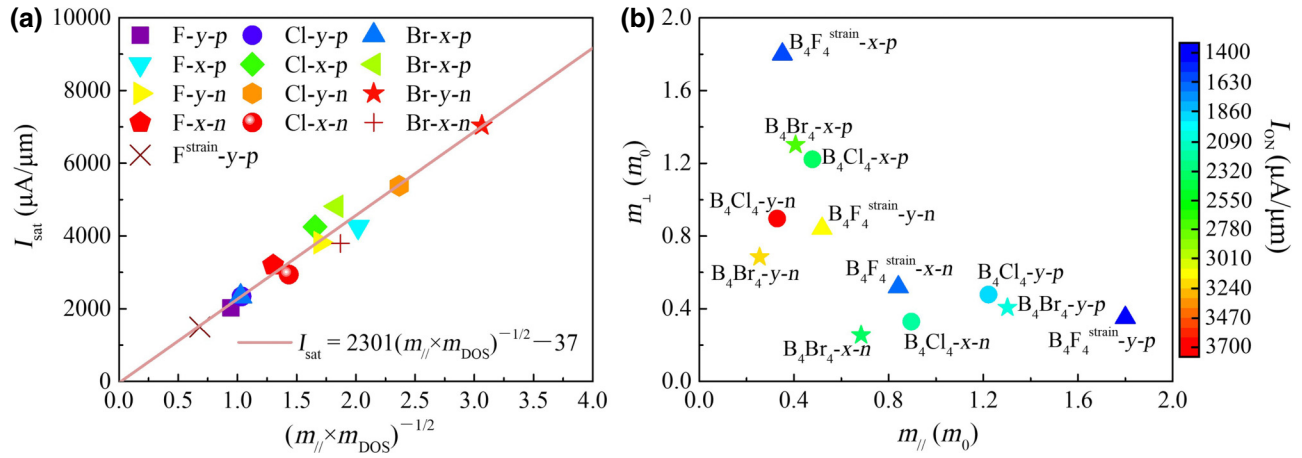
FIG. 4. (a) Saturation current I_{sat} versus $(m_{DOS} \times m_{//})^{-1/2}$ for monolayer B_4X_4 MOSFETs. (b) I_{ON} as a function of $m_{//}$ and $m_{\perp}$.

fixed I_{OFF} and V_{dd} [61]. In relevance to this, the monolayer strained B_4F_4, B_4Cl_4, and B_4Br_4 benefit from the appropriate magnitudes of the band gaps and effective masses, thus achieving small SS and sizable ON-state current that can meet the ITRS requirements for HP devices. The SS of monolayer strained B_4F_4, B_4Cl_4, and B_4Br_4 can be found in Fig. 5(a).

Finally, we characterize the delay time (τ) and the power-delay product (PDP), which are two other metrics for accessing the operation speed and the energy consumption of a transistor in Fig. 5(b). The delay time corresponds to the upper limit of the switching speed in the logic circuit, which is defined as [22,62]

$$\tau = \frac{Q_{ON} - Q_{OFF}}{I_{ON}}, \tag{4}$$

where Q_{ON} and Q_{OFF} represent the charge in the channel in the ON and OFF states, respectively. The PDP represents the power dissipation of a single switching system and is

expressed as

$$PDP = (Q_{ON} - Q_{OFF}) \times V_{ds}. \tag{5}$$

If the τ and PDP are lower, the device performance is better. We calculate the τ and PDP of the monolayer B_4X_4 MOSFETs, as summarized in Table SV within the Supplemental Material [64]. The τ and PDP of all monolayer strained B_4F_4, B_4Cl_4, and B_4Br_4 MOSFETs meet the ITRS requirements for HP devices ($\tau < 0.423$ ps, PDP < 0.24 fJ/μm), thus unraveling their strong potential in ultrascaled MOSFET device technology beyond the silicon era.

Furthermore, it is noted that the PBE functional adopted in this work usually underestimates the band gap. The band-gap underestimation of monolayer B_4F_4 induces the source-to-drain leakage tunneling and thus obvious degrade of SS and I_{ON}. While for monolayer B_4Cl_4 and B_4Br_4, the underestimated band gaps are larger than 1.10 eV. The SS of 5-nm gate-length monolayer B_4Cl_4 and B_4Br_4 MOSFETs are close to the theoretical limit
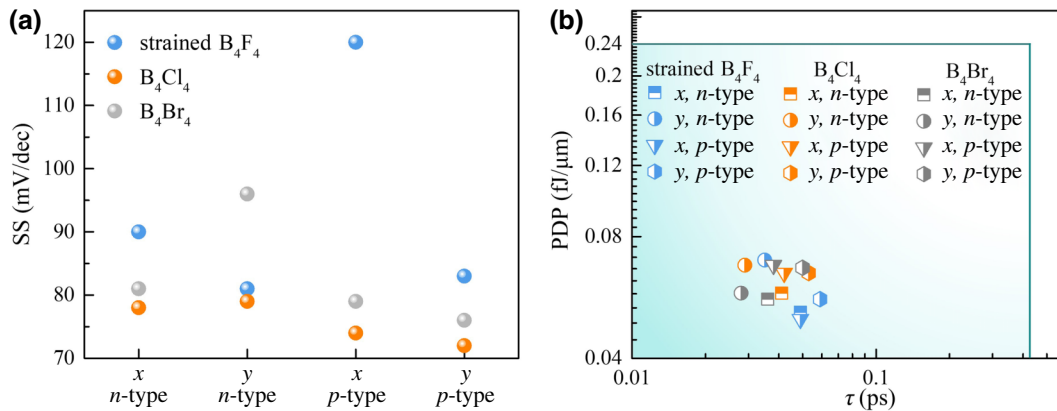

FIG. 5. The (a) SS, (b) τ and PDP of 5-nm gate-length monolayer strained B_4F_4, B_4Cl_4, and B_4Br_4 MOSFETs calculated according to the ITRS HP device standard.

of 60 mV/dec [59]. Therefore, the band-gap underestimation should have little impact on their device performances. Additionally, the device simulations in this work neglect several problems in actual device such as phonon scattering and contact resistance, which will reduce the high I_{ON} of monolayer B_4X_4 MOSFETs. The mean free paths of monolayer B_4X_4 are calculated to be larger than 9 nm for electrons and holes, indicating the ballistic transport in 5-nm gate-length monolayer B_4X_4 MOSFETs with phonon scattering neglected. A Schottky contact with metal-induced gap states (MIGS) and Fermi-level pinning always brings high contact resistance and thus degrades the I_{ON} severely. It is highly desirable to search a suitable electrode to achieve an Ohmic contact with monolayer B_4X_4. Compared with metals, semimetals could suppress MIGS to reduce contact resistance [63]. Further investigations on the contact between semimetals and monolayer B_4X_4 are interesting and necessary.

IV. CONCLUSIONS

In summary, we computationally assess the quantum transport properties of monolayer B_4X_4 by DFT coupled with NEGF method. Monolayer B_4Cl_4 and B_4Br_4 MOSFETs with 5-nm channel length show a high ON-state current due to the suitable band gap and anisotropic electronic structure. However, the ON-state current of 5-nm monolayer B_4F_4 MOSFETs is lower than the HP standard of ITRS because of the small band gap (0.70 eV). By strain engineering, the HP ON-state current of the *n*-type 5-nm monolayer B_4F_4 MOSFET can be increased from 600 to 3140 μA/μm. Furthermore, we identify the relationship between the anisotropic electronic structures and device performances. The electronic anisotropy does not guarantee a high ON-state current. Instead, an intricate balance between the $m_{//}$ or $m_{\perp}$ is needed to ensure good performance. Particularly, the effective mass is overly large, the saturation current can be undesirably suppressed, thus limiting the ON-state current. Our findings reveal the enormous potential of monolayer B_4F_4, B_4Cl_4, and B_4Br_4 in 5-nm channel-length nanoelectronic devices, and shall provide guidance for the identification of excellent 2D channel materials for HP ultrascaled electronic devices.

ACKNOWLEDGMENTS

[1] G. Fiori, F. Bonaccorso, G. Iannaccone, T. Palacios, D. Neumaier, A. Seabaugh, S. K. Banerjee, and L. Colombo, Electronics based on two-dimensional materials, Nat. Nanotechnol. **9,** 768 (2014).

[2] S. Salahuddin, K. Ni, and S. Datta, The era of hyper-scaling in electronics, Nat. Electron. **1,** 442 (2018).

[3] M. Chhowalla, D. Jena, and H. Zhang, Two-dimensional semiconductors for transistors, Nat. Rev. Mater. **1,** 16052 (2016).

[4] S. Zeng, Z. Tang, C. Liu, and P. Zhou, Electronics based on two-dimensional materials: Status and outlook, Nano Res. **14,** 1752 (2020).

[5] A. Pal, S. Zhang, T. Chavan, K. Agashiwala, C. H. Yeh, W. Cao, and K. Banerjee, Quantum-engineered devices based on 2D materials for next-generation information processing and storage, Adv. Mater. **35,** e2109894 (2023).

[6] B. Radisavljevic, A. Radenovic, J. Brivio, V. Giacometti, and A. Kis, Single-layer MoS$_2$ transistors, Nat. Nanotechnol. **6,** 147 (2011).

[7] Sujay B. Desai, A. B. Sachid, Surabhi R. Madhvapathy, Juan Pablo Llinas, Qingxiao Wang, Geun Ho Ahn, Gregory Pitner, Moon J. Kim, Jeffrey Bokor, Chenming Hu, H.-S. Philip Wong, and Ali Javey, MoS$_2$ transistors with 1-nanometer gate lengths, Science **354,** 99 (2016).

[8] D. A. Bandurin, A. V. Tyurnina, G. L. Yu, A. Mishchenko, V. Zolyomi, S. V. Morozov, R. K. Kumar, R. V. Gorbachev, Z. R. Kudrynskyi, S. Pezzini, Z. D. Kovalyuk, U. Zeitler, K. S. Novoselov, A. Patane, L. Eaves, I. V. Grigorieva, V. I. Fal'ko, A. K. Geim, and Y. Cao, High electron mobility, quantum Hall effect and anomalous optical response in atomically thin InSe, Nat. Nanotechnol. **12,** 223 (2017).

[9] E. G. Marin, D. Marian, G. Iannaccone, and G. Fiori, First-principles simulations of FETs based on two-dimensional InSe, IEEE Electron Device Lett. **39,** 626 (2018).

[10] J. Wu, H. Yuan, M. Meng, C. Chen, Y. Sun, Z. Chen, W. Dang, C. Tan, Y. Liu, J. Yin, Y. Zhou, S. Huang, H. Q. Xu, Y. Cui, H. Y. Hwang, Z. Liu, Y. Chen, B. Yan, and H. Peng, High electron mobility and quantum oscillations in non-encapsulated ultrathin semiconducting Bi$_2$O$_2$Se, Nat. Nanotechnol. **12,** 530 (2017).

[11] L. K. Li, Y. J. Yu, G. J. Ye, Q. Q. Ge, X. D. Ou, H. Wu, D. L. Feng, X. H. Chen, and Y. B. Zhang, Black phosphorus field-effect transistors, Nat. Nanotechnol. **9,** 372 (2014).

[12] C. Xi and G. Jing, Simulation of phosphorene field-effect transistor at the scaling limit, IEEE Trans. Electron Devices **62,** 659 (2015).

[13] H. Qu, S. Guo, W. Zhou, and S. Zhang, Uncovering the anisotropic electronic structure of 2D group VA-VA monolayers for quantum transport, IEEE Electron Device Lett. **42,** 66 (2021).

[14] S. Guo, Y. Zhang, Y. Ge, S. Zhang, H. Zeng, and H. Zhang, 2D V-V binary materials: Status and challenges, Adv. Mater. **31,** 1902352 (2019).

[15] W. Zhou, S. Zhang, Y. Wang, S. Guo, H. Qu, P. Bai, Z. Li, and H. Zeng, Anisotropic in-plane ballistic transport in monolayer black arsenic-phosphorus FETs, Adv. Electron. Mater. **6,** 1901281 (2020).

[16] Y. Fang, F. Wang, R. Wang, T. Zhai, and F. Huang, 2D NbOI$_2$: A chiral semiconductor with highly in-plane anisotropic electrical and optical properties, Adv. Mater. **33,** e2101505 (2021).

[17] T. Su, C. H. Lee, S. D. Guo, G. Wang, W.-L. Ong, L. Cao, W. Zhao, S. A. Yang, and Y. S. Ang, 2D Janus niobium oxydihalide NbOXY: Multifunctional piezoelectric semiconductor for electronics, photonics, sensing and sustainable energy applications, Mater. Today Phys. **31,** 101001 (2023).

[18] Y. Jia, M. Zhao, G. Gou, X. C. Zeng, and J. Li, Niobium oxide dihalides NbOX$_2$: A new family of two-dimensional van der Waals layered materials with intrinsic ferroelectricity and antiferroelectricity, Nanoscale Horiz. **4,** 1113 (2019).

[19] Y. Wu, I. Abdelwahab, K. C. Kwon, I. Verzhbitskiy, L. Wang, W. H. Liew, K. Yao, G. Eda, K. P. Loh, L. Shen, and S. Y. Quek, Data-driven discovery of high performance layered van der Waals piezoelectric NbOI$_2$, Nat. Commun. **13,** 1884 (2022).

[20] A. Zavabeti, P. Aukarasereenont, H. Tuohey, N. Syed, A. Jannat, A. Elbourne, K. A. Messalea, B. Y. Zhang, B. J. Murdoch, J. G. Partridge, M. Wurdack, D. L. Creedon, J. van Embden, K. Kalantar-Zadeh, S. P. Russo, C. F. McConville, and T. Daeneke, High-mobility p-type semiconducting two-dimensional β-TeO$_2$, Nat. Electron. **4,** 277 (2021).

[21] S. Guo, H. Qu, W. Zhou, S. A. Yang, Y. S. Ang, J. Lu, H. Zeng, and S. Zhang, High-performance and low-power transistors based on anisotropic monolayer β-TeO$_2$, Phys. Rev. Appl. **17,** 064010 (2022).

[22] S. Guo, W. Zhou, H. Qu, S. Zhang, W. Liu, G. Liu, X. Xia, X. Song, and H. Zeng, Quantum transport in monolayer α-CS field-effect transistors, Adv. Electron. Mater. **7,** 2001169 (2021).

[23] R. Quhe, Q. Li, Q. Zhang, Y. Wang, H. Zhang, J. Li, X. Zhang, D. Chen, K. Liu, Y. Ye, L. Dai, F. Pan, M. Lei, and J. Lu, Simulations of quantum transport in sub-5-nm monolayer phosphorene transistors, Phys. Rev. Appl. **10,** 024022 (2018).

[24] S. Zhang, S. Guo, Z. Chen, Y. Wang, H. Gao, J. Gomez-Herrero, P. Ares, F. Zamora, Z. Zhu, and H. Zeng, Recent progress in 2D group-VA semiconductors: From theory to experiment, Chem. Soc. Rev. **47,** 982 (2018).

[25] X. Wu, J. Dai, Y. Zhao, Z. Zhuo, J. Yang, and X. C. Zeng, Two-dimensional boron monolayer sheets, ACS Nano **6,** 7443 (2012).

[26] A. J. Mannix, X. F. Zhou, B. Kiraly, J. D. Wood, D. Alducin, B. D. Myers, X. Liu, B. L. Fisher, U. Santiago, J. R. Guest, M. J. Yacaman, A. Ponce, A. R. Oganov, M. C. Hersam, and N. P. Guisinger, Synthesis of borophenes: Anisotropic, two-dimensional boron polymorphs, Science **350,** 1513 (2015).

[27] Z. Zhang, E. S. Penev, and B. I. Yakobson, Two-dimensional boron: Structures, properties and applications, Chem. Soc. Rev. **46,** 6746 (2017).

[28] B. Feng, J. Zhang, Q. Zhong, W. Li, S. Li, H. Li, P. Cheng, S. Meng, L. Chen, and K. Wu, Experimental realization of two-dimensional boron sheets, Nat. Chem. **8,** 563 (2016).

[29] E. S. Penev, S. Bhowmick, A. Sadrzadeh, and B. I. Yakobson, Polymorphism of two-dimensional boron, Nano Lett. **12,** 2441 (2012).

[30] X. Liu, L. Wang, B. I. Yakobson, and M. C. Hersam, Nanoscale probing of image-potential states and electron transfer doping in borophene polymorphs, Nano Lett. **21,** 1169 (2021).

[31] W. Li, L. Kong, C. Chen, J. Gou, S. Sheng, W. Zhang, H. Li, L. Chen, P. Cheng, and K. Wu, Experimental realization of honeycomb borophene, Sci. Bull. **63,** 282 (2018).

[32] X. Tang, J. Gu, J. Shang, Z. Chen, and L. Kou, Double-sided surface functionalization: An effective approach to stabilize and modulate the electronic structure of graphene-like borophene, InfoMat **3,** 327 (2020).

[33] P. Habibi, T. J. H. Vlugt, P. Dey, and O. A. Moultos, Reversible hydrogen storage in metal-decorated honeycomb borophene oxide, ACS Appl. Mater. Interfaces **13,** 43233 (2021).

[34] L. Yan, P. F. Liu, H. Li, Y. Tang, J. He, X. Huang, B. T. Wang, and L. Zhou, Theoretical dissection of superconductivity in two-dimensional honeycomb borophene oxide B$_2$O crystal with a high stability, npj Comput. Mater. **6,** 94 (2020).

[35] Y. An, Y. Hou, H. Wang, J. Li, R. Wu, T. Wang, H. Da, and J. Jiao, Unveiling the electric-current-limiting and photodetection effect in two-dimensional hydrogenated borophene, Phys. Rev. Appl. **11,** 064031 (2019).

[36] H. Nishino, T. Fujita, N. T. Cuong, S. Tominaka, M. Miyauchi, S. Iimura, A. Hirata, N. Umezawa, S. Okada, E. Nishibori, A. Fujino, T. Fujimori, S. I. Ito, J. Nakamura, H. Hosono, and T. Kondo, Formation and characterization of hydrogen boride sheets derived from MgB$_2$ by cation exchange, J. Am. Chem. Soc. **139,** 13761 (2017).

[37] A. Fujino, S. I. Ito, T. Goto, R. Ishibiki, J. N. Kondo, T. Fujitani, J. Nakamura, H. Hosono, and T. Kondo, Hydrogenated borophene shows catalytic activity as solid acid, ACS Omega **4,** 14100 (2019).

[38] M. Shahrokhi, Can fluorine and chlorine functionalization stabilize the graphene like borophene?, Comp. Mater. Sci. **156,** 56 (2019).

[39] J. P. Perdew, K. Burke, and M. Ernzerhof, Generalized gradient approximation made simple, Phys. Rev. Lett. **77,** 3865 (1996).

[40] H. J. Monkhorst and J. D. Pack, Special points for Brillouin-zone integrations, Phys. Rev. B **13,** 5188 (1976).

[41] M. Brandbyge, J. L. Mozos, P. Ordejón, J. Taylor, and K. Stokbro, Density-functional method for nonequilibrium electron transport, Phys. Rev. B **65,** 165401 (2002).

[42] S. Datta, *Quantum Transport: Atom to Transistor* (Cambridge University Press, Cambridge, 2005).

[43] S. Datta, *Electronic Transport in Mesoscopic Systems* (Cambridge University Press, Cambridge, 1995). Cambridge Studies in Semiconductor Physics and Microelectronic Engineering.

[44] S. Smidstrup, *et al.*, QuantumATK: An integrated platform of electronic and atomic-scale modelling tools, J. Phys.: Condens. Matter **32,** 015901 (2020).

[45] L. C. Xu, A. Du, and L. Kou, Hydrogenated borophene as a stable two-dimensional Dirac material with an ultra-high Fermi velocity, Phys. Chem. Chem. Phys. **18**, 27284 (2016).

[46] H. Tang and S. Ismail-Beigi, Novel precursors for boron nanotubes: The competition of two-center and three-center bonding in boron sheets, Phys. Rev. Lett. **99**, 115501 (2007).

[47] K. T. Lam, Z. Dong, and J. Guo, Performance limits projection of black phosphorous field-effect transistors, IEEE Electron Device Lett. **35**, 963 (2014).

[48] G. Pizzi, M. Gibertini, E. Dib, N. Marzari, G. Iannaccone, and G. Fiori, Performance of arsenene and antimonene double-gate MOSFETs from first principles, Nat. Commun. **7**, 12585 (2016).

[49] International technology roadmap for semiconductors, www.itrs2.net.

[50] Y. Wang, P. Huang, M. Ye, R. Quhe, Y. Pan, H. Zhang, H. Zhong, J. Shi, and J. Lu, Many-body effect, carrier mobility, and device performance of hexagonal arsenene and antimonene, Chem. Mater. **29**, 2191 (2017).

[51] M. C. Robbins and S. J. Koester, Black phosphorus p- and n-MOSFETs with electrostatically doped contacts, IEEE Electron Device Lett. **38**, 285 (2017).

[52] M. Buscema, D. J. Groenendijk, G. A. Steele, H. S. van der Zant, and A. Castellanos-Gomez, Photovoltaic effect in few-layer black phosphorus PN junctions defined by local electrostatic gating, Nat. Commun. **5**, 4651 (2014).

[53] Y. Zhao, K. Xu, F. Pan, C. Zhou, F. Zhou, and Y. Chai, Doping, contact and interface engineering of two-dimensional layered transition metal dichalcogenides transistors, Adv. Funct. Mater. **27**, 1603484 (2016).

[54] S. P. Koenig, R. A. Doganov, L. Seixas, A. Carvalho, J. Y. Tan, K. Watanabe, T. Taniguchi, N. Yakovlev, A. H. Castro Neto, and B. Ozyilmaz, Electron doping of ultrathin black phosphorus with Cu adatoms, Nano Lett. **16**, 2145 (2016).

[55] D. Xiang, C. Han, J. Wu, S. Zhong, Y. Liu, J. Lin, X. A. Zhang, W. Ping Hu, B. Ozyilmaz, A. H. Neto, A. T. Wee, and W. Chen, Surface transfer doping induced effective modulation on ambipolar characteristics of few-layer black phosphorus, Nat. Commun. **6**, 6485 (2015).

[56] J. Huang and J. Kang, Defect and doping properties of two-dimensional $PdSe_2$, J. Phys. Chem. C **126**, 20678 (2022).

[57] D. Wang, X. B. Li, and H. B. Sun, Modulation doping: A strategy for 2D materials electronics, Nano Lett. **21**, 6298 (2021).

[58] F. Schwierz, J. Pezoldt, and R. Granzner, Two-dimensional materials and their prospects in transistor electronics, Nanoscale **7**, 8261 (2015).

[59] F. Liu, C. Qiu, Z. Zhang, L.-M. Peng, J. Wang, and H. Guo, Dirac electrons at the source: Breaking the 60-mV/decade switching limit, IEEE Trans. Electron Devices **65**, 2736 (2018).

[60] S. Takagi, in *2003 Symposium on VLSI Technology. Digest of Technical Papers (IEEE Cat. No.03CH37407)*, Kyoto, Japan, (2003), pp. 115.

[61] W. Cao, H. Bu, M. Vinet, M. Cao, S. Takagi, S. Hwang, T. Ghani, and K. Banerjee, The future transistors, Nature **620**, 501 (2023).

[62] S. Guo, Y. Wang, X. Hu, S. Zhang, H. Qu, W. Zhou, Z. Wu, X. Liu, and H. Zeng, Ultrascaled double-gate mono-layer SnS_2 MOSFETs for high-performance and low-power applications, Phys. Rev. Appl. **14**, 044031 (2020).

[63] P. C. Shen, *et al.*, Ultralow contact resistance between semimetal and monolayer semiconductors, Nature **593**, 211 (2021).

[64] See Supplemental Material at http://link.aps.org/supplemental/10.1103/PhysRevApplied.21.054016 for the atomic structure and band structure of graphenelike borophene, phonon band structures for monolayer B_4X_4, transfer characteristics of the MOSFETs based on monolayer B_4F_4 and strained B_4F_4, and other calculation results.